A Transient Stiffness Measure for Islanding Detection of Multi-DG Systems

Mohamed Al Hosani , *Member, IEEE*, Zhihua Qu , *Fellow, IEEE*, and H. H. Zeineldin , *Senior Member, IEEE*

Abstract—**Islanding detection is important to ensure the reliability and safety of distributed generation (DG). In this paper, a new active islanding detection method (IDM) is proposed, and it depends on individually estimating an overall transient stiffness measure for any multi-DG system to establish a clear separation between prior- and post-islanding stiffness. For the multi-DG system to avoid spectrum overlapping, each of its DGs is required to perturb at distinct frequencies. By using this concept of perturbation separation, the proposed technique can be applied to multi-DG systems without requiring any communication among the DGs. Simulation results show that the proposed technique is scalable and robust against different loading conditions and variations of grid stiffness levels as well as with respect to the number of connected DGs and different types of DG controllers. It is also shown that the proposed technique can successfully distinguish islanding conditions from other disturbances that may occur in power system networks.**

Index Terms—**Distributed generation (DG), islanding detection, quality factor, stiffness, transient response.**

I. INTRODUCTION

VARIOUS islanding detection methods (IDMs) have been developed within the last 15 years in anticipation of the tremendous increase in the penetration of distributed generation (DG) in distribution systems [1], [2]. Active IDMs, which rely on injecting small perturbations to enhance the voltage/frequency drifting behavior caused by losing grid connectivity, have been of great interest to protection engineers due to their high performance-to-cost ratio [3]–[7]. However, active techniques raise stability concerns since the injected disturbance is a destabilizing force in general [8], [9]. Another important issue with active IDMs is scalability where different active IDMs

might degrade the performance of each other in multi-DG systems [10]–[12]. Moreover, the interaction between active IDMs and different interface controls has been of concern for protection engineers and researchers [13]–[15]. In [14] and [15], it is shown that the Sandia frequency shift (SFS), which is a well-known active IDM, is more effective for a constant current-controlled inverter in comparison to a constant power-controlled inverter where the latter controller counter effects the perturbation introduced by SFS.

Small-signal stability analysis has been implemented to study the effect of adding inverter-based DGs on distribution networks stability in addition to the contribution of implemented control and IDM schemes in single and multi-DG system stability [16]–[18]. In [18], a detailed small-signal analysis is used to study the effect of different IDMs on the stability of single and multi-DG systems under constant current and constant power controllers. Constant current/power controllers are useful for DGs working in the grid-connected mode while stand alone or microgrid operation is considered as a major drawback for the aforementioned control schemes. This is mainly because the constant current and constant power controllers do not provide the appropriate power-management strategy (PMS), required to support the voltage and the frequency within the microgrid. In [19] and [20], switching control strategies are proposed to support the voltage of the microgrid in the stand-alone mode. The problem with these techniques is that a large transient/oscillation is introduced as a result of switching between different modes of control. Alternatively, droop controllers, which replicate the droop characteristic of synchronous generators, are proposed for power-management strategies or as a power-sharing mechanism [16], [21]–[23]. In [16], an active/reactive PMS is proposed, and it includes a frequency restoration term, and frequency/voltage droop blocks, in addition to the typical power regulator. In this paper, the PMS proposed in [16] is utilized in the multi-DG model to develop a new active IDM that is suitable for different control schemes including microgrid PMSs.

This paper proposes a new active IDM for a multi-DG system such that no communication is required among different DGs. The proposed technique is based on the idea of transient stiffness measurement for the multi-DG system where a clear separation is established between prior- and post-islanding stiffness measures. The idea originates from a simple mass-spring-damper system and is extended to the multi-DG system. A small-signal model for the multi-DG system is developed and used for simulation along with an equivalent average Simulink model. The proposed technique is suitable for different types of DG controllers and is shown to be robust against different types of power system disturbances.

Fig. 1. General multi-DG system under study.

Fig. 2. Mass-spring-damper system.
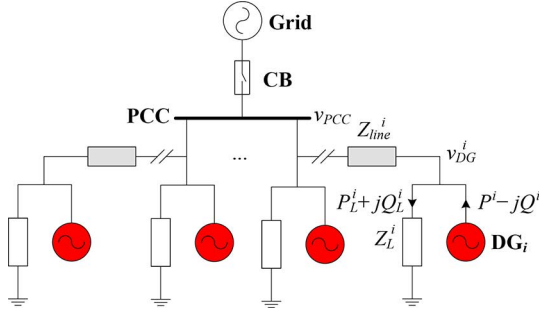
II. MULTI-DG SYSTEM UNDER STUDY

A general multi-DG system is shown in Fig. 1. In Fig. 1, the output power of the ith DG is $P^i - jQ^i$. The negative sign in the reactive power indicates that Q^i is the reactive power absorbed by the ith DG. The point of common coupling (PCC) voltage is v_{PCC}, and v_{DG}^i is the ith DG bus voltage. A circuit breaker (CB) is used to simulate an islanding situation by disconnecting the multi-DG system from the grid. A phase-locked loop (PLL) is used to measure the frequency of the DG bus voltage. The interface control used for each DG includes a current regulator in addition to the PMS introduced in [16]. The small-signal model for a multi-DG system is derived in the Appendix.

III. PROPOSED DESIGN

The idea behind the proposed technique is to introduce a mathematical measure of transient stiffness for multi-DG systems such that, through online identification and calculation of that measure, a clear separation is established for the prior- and post-islanding values of the stiffness measure. First, the stiffness concept is introduced for dynamical systems. Then, the concept is applied to multi-DG systems.

A. Stiffness Measure of Dynamical Systems

To define the stiffness concept for a dynamic system, consider first the mass-spring-damper system in Fig. 2, where m is the body mass, k_s is the spring constant, d is the damping coefficient, and $f(t)$ is the applied force. Applying Newton's second law to the system yields the spring damper model

$$m\ddot{x} = -k_s x - d\dot{x} + mf(t) \tag{1}$$

where x is the displacement. It follows that the transfer function is given by $H(s) = X(s)/F(s)$

$$H(s) = \frac{1}{s^2 + ds/m + k_s/m},$$
$$sH(s) = \frac{s}{s^2 + ds/m + k_s/m} \tag{2}$$

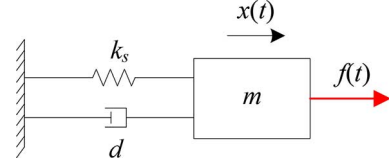where s is the Laplace operator, and $X(s)$ and $F(s)$ are the Laplace transform of $x(t)$ and $f(t)$, respectively. Then, the infinity-norm of (2) can be obtained as follows: The normalized spring constant k_s/m is known to be the stiffness. Therefore, for a dynamical system of transfer function $H(s)$, its "stiffness measure" and "damping" can be calculated analogously as k_s/m and d/m in (3), shown at the bottom of the page; that is, the stiffness measure (S) and damping (D) are calculated as

$$S = \left(\frac{\|sH(s)\|_\infty}{\|H(s)\|_\infty} \right)^2 + \frac{1}{4\|sH(s)\|_\infty^2} \approx \left(\frac{\|sH(s)\|_\infty}{\|H(s)\|_\infty} \right)^2, \tag{4}$$

$$D = 1/\|sH(s)\|_\infty.$$

In the event that system damping (D) satisfies the inequality of $D \geq \sqrt{2S}$, S is reset to $1/\|H(s)\|_\infty$.

B. Stiffness Measure for a Multi-DG System

From the basic principle of power flow, the following transfer function is now considered:

$$H_\omega^i(s) = \frac{\Delta\omega_p^{'i}(s)}{\Delta P_o^i(s)} \tag{5}$$

where $\omega_p^{'i} = \omega_p^i/\omega_g$, ω_p is the angular frequency of the ith DG terminal voltage acquired by PLL, ω_g is the grid nominal angular frequency, Δ is the small-signal variable, and ΔP_o^i is the ith DG variation in input active power. For a single DG system, one can easily design for ΔP_o such that the measured ω_p is used to identify H_ω. Then, stiffness of the single DG system can be found according to (4). However, for a multi-DG system, the problem becomes more complicated due to spectral overlapping in ω_p as a result of perturbation injections by each of DGs separately. Hence, the problem that should be addressed is how to design injection(s) for ΔP_o^i such that an overall measure of stiffness can be found from ω_p^i without any communication among different DGs. The specific idea proposed in this paper relies on the concept of separate frequencies in the discrete Fourier transform (DFT) to solve for an overall stiffness measure for the multi-DG system.

The input perturbation ΔP_o^i for the ith DG is designed as

$$\Delta P_o^i[n] = \frac{A}{M} \sum_{\mu=1}^{M} \cos\left(\omega_\mu^i(n-1)T_s\right) \tag{6}$$

$$\|H(s)\|_\infty = \begin{cases} m/k_s, & d \geq \sqrt{2mk_s} \\ \frac{2m^2}{d\sqrt{4mk_s - d^2}}, & d < \sqrt{2mk_s} \end{cases}, \qquad \|sH(s)\|_\infty = \frac{m}{d}. \tag{3}$$
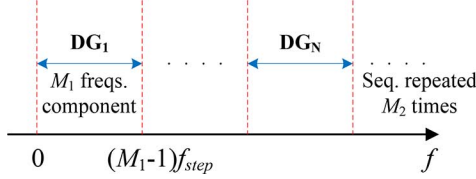
Fig. 3.   Separation of frequency injection for multi-DG inputs.

where $n = 1, 2, \ldots, N_T, \omega_\mu^i = 2\pi f_\mu^i, f_\mu^i = [k_1 + M_1(Nk_2 + i - 1)]f_{\text{step}}, T_s = 1/f_s$ is the data sampling interval, A is the perturbation amplitude, $k_1 = 0, 1, \ldots, M_1 - 1, k_2 = 0, 1, \ldots, M_2 - 1, M_1$ is the number of consecutive frequencies disturbed by the ith DG, $M_2 = \text{floor}((f_u + f_{\text{step}})/NM_1 f_{\text{step}}), f_u$ is the maximum frequency injected by the input, and $M = M_1 M_2$. The separation in the DFT of input frequency components for each DG is shown in Fig. 3. It can be seen from Fig. 3 that the first M_1 frequency components are injected by DG_1, the second M_1 frequency components are injected by DG_2, and so on up to the Nth DG. The disturbed bands for each of the DGs are separated by f_{step} to avoid overlapping between different DGs' spectral components. Then, the sequence is repeated M_2 times to cover the entire region between 0 and f_u. The only global information needed for this scheme is the maximum number of DGs, N; and all of the possible DGs are indexed during their installation.

The design parameters in the proposed scheme in (6) are $f_u, f_{\text{step}}, f_s, N_T, A$, and M_1. The relation between some of those design parameters and design conditions can be obtained from DFT properties, practical considerations, and the uniform band-pass sampling theorem [24]. According to [24], the minimum sampling frequency to avoid aliasing for a single band-pass signal, with a center frequency located at $0.5 f_u$, is the Nyquist sampling rate. Hence, f_s should be chosen to be greater than or equal to $2 f_u$. For convenience, f_s is chosen to be 7.68 kHz which corresponds to 128 samples/cycle at 60 Hz. Let us assume that the time interval for collecting data (T) is fixed to 0.1 s. Then, N_T is equal to $f_s T = 768$ points. By fixing the value of T, the minimum frequency resolution of input DFT is also fixed to $1/T = 10$ Hz. Thus, f_{step} is set to 10 Hz. In addition, let us assume that the frequency region of interest for calculating the ∞-norm is $[f_0, f_c]$, where f_0 is set to 60 Hz and f_c is equal to 0.5 kHz. Then, f_u is chosen to be $5 f_c = 2.5$ kHz in order to have more frequency components in the DFT and, hence, higher accuracy for $\hat{H}_\omega$. The choices of f_0 and f_c are chosen using the physical knowledge of the system and can be verified via simulation. The choice of M_1 value is critically important and, hence, it will be studied further in Section IV. The perturbation amplitude is set to one $(A = 1)$.

Once again, the proposed scheme only requires the knowledge of the maximum number of DGs (N), and DGs are assigned a unique index number within the microgrid of interest. Then, the following procedure can be used to estimate the overall stiffness measure:1) the perturbation input $\Delta P_o^i[n]$, defined in (6), is injected by the ith DG where $n = 1, 2, \ldots, N_T$, and $i = 1, 2, \ldots, N$; 2) for the ith DG, measure $\omega_p^i[n]$ where $n = 1, 2, \ldots, N_T$; 3) ω_p^i is normalized by ω_g and then the

dc component is removed by subtracting one to obtain $\Delta \omega_p'^i$; 4) apply the DFT on $\Delta \omega_p'^i[n]$ to obtain $\Delta W_p^i(j\omega_k)$, where $\omega_k = 2\pi(k - 1)f_k/N_T$ and $k = 1, 2, \ldots, N_T$; and 5) the estimated overall frequency response over the region of interest is given by

$$\hat{H}_\omega^i(j\omega_l) = \frac{2M}{A} \Delta W_p^i(j\omega_l) \qquad (7)$$

where $\omega_l = 2\pi f_l$ and $f_l \epsilon [f_0, f_c]$, and 6) the estimated stiffness for the overall multi-DG system in decibels is calculated as follows:

$$\hat{S}_\omega^i(\text{dB}) = 20 \log_{10} \left(\frac{\max\limits_{\omega_l} \omega_l \left| \hat{H}_\omega^i(j\omega_l) \right|}{\max\limits_{\omega_l} \left| \hat{H}_\omega^i(j\omega_l) \right|} \right). \qquad (8)$$

It is worth noting that (8) can be applied to an arbitrary system of any order as long as its frequency response can be obtained. Given that the system model can be approximated by some second-order transfer function (which is a well-known fact in the field of system identification and order reduction), the outcome of (8) would be its stiffness value.

In practice, an additional low-pass filtering stage could be applied to $\omega_p^i[n]$ at step 3 of the aforementioned procedure to remove high-frequency harmonics and noise. Then, the filter response should be accounted for in (7) to calculate the correct $\hat{H}_\omega^i$. The previous process is repeated every T second. Then, the proposed stiffness-measure IDM is defined as

$$\begin{cases} \hat{S}_\omega^i \leq S_{\text{TH}}, & \text{Islanding is detected by DG}_i \\ \hat{S}_\omega^i > S_{TH}, & \text{Normal operation} \end{cases} \qquad (9)$$

where S_{TH} is the stiffness threshold value in decibels that separates islanding from nonislanding conditions. S_{TH} is designed such that the proposed IDM is robust against different loading conditions, variations in grid stiffness level, number of connected DGs, and different types of power system disturbances. In this paper, S_{TH} is set equal to 59 dB. Alternatively, an optimization technique could be used to find the optimum threshold that provides the best separation between prior- and post-islanding stiffness values for all practical variations in both loads and the grid. The theoretical stiffness measure for the N-DG system is defined as

$$S_\omega(\text{dB}) = \frac{1}{N} \sum_{i=1}^{N} 20 \log_{10} \left(\frac{\max\limits_{\omega \in [\omega_0, \omega_c]} \left| H_\omega^i(j\omega) \right|}{\max\limits_{\omega \in [\omega_0, \omega_c]} \left| H_\omega^i(j\omega) \right|} \right) \qquad (10)$$

where $\omega_0 = 2\pi f_0$ and $\omega_c = 2\pi f_c$. Measure S_ω is not known, and $\hat{S}_\omega^i$ is the estimate of S_ω by DG_i.

IV. SIMULATION RESULTS

The proposed stiffness-measure IDM in Section III is verified using an average model implemented in MATLAB Simulink. The detail of the model can be found in the Appendix. For illustration purposes, the results for single and two-DG systems are considered and the concept can be easily extended to the general N-DG system. Unless mentioned otherwise, the model
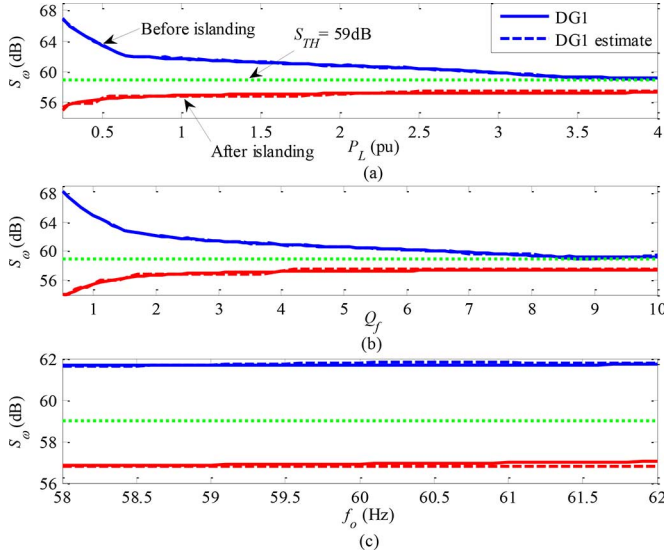
Fig. 4. S_ω (solid) and $\hat{S}_\omega$ (dashed) before (blue) and after (red) islanding. (a) P_L changes. (b) Q_f changes. (c) f_o changes.

parameters, introduced in Table I in the Appendix, is used for simulation. The base power is 10 kVA.

A. Sensitivity Study for a Single DG System

The purpose of this study is to understand the effect of important parameters on the stiffness measure for a single DG system. The small-signal model, developed in the Appendix, is used for sensitivity analysis. The stiffness measure obtained from an ideal H_ω is compared with the estimated one obtained from $\hat{H}_\omega$. Three factors are investigated in this subsection which includes: the load parameters, the distribution line impedance, and the maximum levels of power. The range of variation for each parameter is chosen such that the stability of the single DG system is maintained before and after islanding condition.

1) Load Parameters: The RLC load parameters include load power level (P_L), load quality factor (Q_f), and load resonant frequency (f_o). These parameters are changed one at a time while the others are kept constant. The parallel RLC load parameters provided in Table I correspond to a 10 kW load with $f_o = 60$ Hz and $Q_f = 2.5$. Fig. 4 shows the actual (S_ω) and estimated $(\hat{S}_\omega)$ stiffness measure before and after islanding for different load parameters. It can be seen from Fig. 4(a) that as P_L increases, the value of S_ω before islanding decreases while it increases after islanding. As the value of P_L increases, the reactive power of both the capacitance and inductance increases accordingly to maintain a constant load Q_f value. The stiffness measure before islanding depends on the exchange of power between the load and the grid as well as the reactive power exchange between the capacitive and inductive parts of the load. When P_L increases, the grid will respond by injecting more active power and, hence, a higher stiffness measure should be obtained. However, the exchange of higher reactive power within the load will have a higher negative impact on the stiffness and, hence, the overall stiffness of the system will decrease. On the other hand, the stiffness measure after islanding depends on the interaction between the PMS and the load, and the characteristics of the RLC load. Therefore, as the value of P_L increases

after islanding, the DG will respond by injecting higher active power and, hence, the overall stiffness will increase. The stiffness gap, between $\hat{S}_\omega$ values for prior- and post-islanding condition, changes from 11.79 to 1.58 dB as P_L is increased from 0.25 to 4 p.u., respectively. From Fig. 4(a), a threshold value of 59 dB provides a clear separation between prior- and post-islanding regions and, hence, the value of S_{TH} is set to 59 dB. The threshold of 59 dB provides consistent separation between prior- and post-islanding stiffness values for all load variations within $\pm400\%$ of the load's rated active power at $Q_f = 2.5$ and $f_o = 60$ Hz. The difference between $\hat{S}_\omega$ and S_ω is a result of the 10 Hz resolution used for calculating $\|\hat{H}_\omega\|_\infty$ where a maximum absolute error (MAE) of 0.38 dB is obtained for all simulated cases. Fig. 4(b) shows that as the Q_f value increases, the stiffness measure before islanding decreases while it increases after islanding. As the load Q_f value increases, the load capacitive and inductive parts exchange higher reactive power and, hence, lower S_ω value is obtained before islanding. On the other hand, RLC loads with higher Q_f values reveal higher resistance to perturbation after islanding and, hence, the S_ω value is increased. At Q_f values equal to 0.5 and 10, the stiffness gap is 14.22 and 1.88 dB, respectively. The 59 dB threshold provides appropriate classification of islanding condition for Q_f values up to 8.5 at $P_L = 1$ p.u. and $f_o = 60$ Hz, where $\hat{S}_\omega$ slightly crosses the threshold of 59 dB afterwards. According to the IEEE Standard 1547, typical load's Q_f values are lower and do not exceed 1 and, hence, the proposed technique can accurately detect islanding for all practical loads [2]. Fig. 4(c) shows that for f_o values below 60 Hz (capacitive load), a lower S_ω is obtained while f_o values above 60 Hz (inductive load) resulted into a higher S_ω value. In the capacitive load case, the grid responds by absorbing a higher reactive power and, hence, the value of S_ω decreases as the load becomes more capacitive. In contrast, the grid injects more reactive power as the load becomes more inductive and the value of S_ω increases accordingly. However, the change of S_ω values is small for all values of f_o within the tested range, and a larger range of f_o could result into unstable operating point after islanding due to the inability of PMS to support the microgrid frequency.

2) Distribution Line Impedance: The distribution system line impedance is an important factor that will significantly affect S_ω value. Stronger grid can be represented either by lower grid impedance magnitude (Z_g) or lower X_g/R_g ratio. The parameters in Table I correspond to $Z_g = 0.2\ \Omega$, and $X_g/R_g = 1.5$. Parameters are changed one at a time while others are kept constant. Fig. 5 shows the effect of X_g/R_g ratio and Z_g value on both S_ω and $\hat{S}_\omega$ before and after islanding. Results in Fig. 5 show that a weaker grid, which corresponds to higher X_g/R_g ratio or higher Z_g value, resulted in a lower stiffness measure and, hence, reducing the separation gap between prior- and post-islanding stiffness measures. The gap shrinks from 9.43 to 3.73 dB as X_g/R_g ratio changes from 0.3 to 10, respectively, while it changes from 9.8 to 0.82 dB as Z_g value changes from 0.05 to 0.8 Ω, respectively. The results in Fig. 5 show that the 59 dB threshold provides appropriate classification of islanding condition for Z_g values up to 0.54 Ω at $X_g/R_g = 1.5$ or any practical range of X_g/R_g ratio at $Z_g = 0.2\ \Omega$. In general, Z_g is typically low for a reliable grid and, hence, the
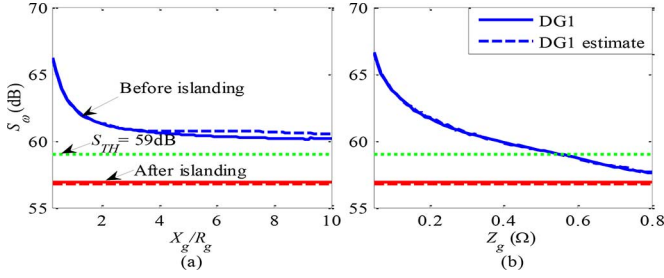
Fig. 5. S_ω (solid) and $\hat{S}_\omega$ (dashed) before (blue) and after (red) islanding. (a) $Z_g = 0.2\Omega$, X_g/R_g changes. (b) $X_g/R_g = 1.5$, Z_g changes.
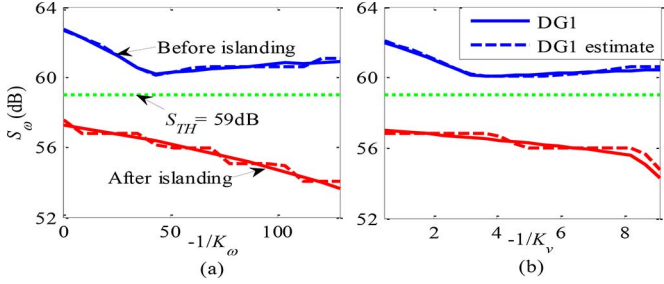

Fig. 6. S_ω (solid) and $\hat{S}_\omega$ (dashed) before (blue) and after (red) islanding. (a) $K_v = -1.1$, K_ω changes. (b) $K_\omega = -0.058$, K_v changes.

Fig. 7. MSE versus M_1 for different numbers of connected DGs.

Fig. 8. $\hat{S}_\omega$ versus m' for a 2-DG system before (solid) and after (dashed) islanding with the PMS employed at DG1 only. (a) $k_{pp}^2 = 0.5$, Q_f changes. (b) $Q_f = 2.5$, k_{pp}^2 changes.

proposed technique provides robust performance for a very wide range of Z_g values and X_g/R_g ratios.

3) Effect of Droop Gains: In this subsection, the effect of using different droop gains ($-1/K_\omega$ and $-1/K_v$) is studied and Fig. 6 shows the effect of different K_ω and K_v values on the stiffness measure before and after islanding. As the droop gains increase, a larger weight is applied to the frequency/voltage error which negatively affects the stiffness measure and a smaller S_ω value is obtained. However, as the droop gain values increase further, the priorislanding value of S_ω starts increasing afterwards since droop gains after a certain threshold will have positive impact on the stiffness value. In contrast, higher droop gains after islanding will always result in lower S_ω values. Furthermore, other parameters, such as PLL proportional gain (k_{pPLL}), could have a significant influence on S_ω, where S_ω decreases as k_{pPLL} increases. As can be seen from the above results, the proposed stiffness measure provides an effective parameter to distinguish any islanding condition.

B. Effect of Load Share Ratio

The input design parameter M_1, presented in (6), should first be optimized for the multi-DG system. As mentioned in Section III, M_1 corresponds to the number of consecutive frequencies disturbed by the ith DG. The mean squared error (MSE) of stiffness measure is optimized and the load Q_f value is changed from 1 to 5 at a step of 0.2. The resulting MSE is

$$\text{MSE} = \frac{1}{N_Q} \sum_{\tau=1}^{N_Q} \left(\frac{1}{N} \sum_{i=1}^{N} \hat{S}_\omega^i(\tau) - S_\omega(\tau) \right)^2 \quad (11)$$

where N_Q is the number of different Q_f values used for calculating MSE. For the two-DG system, the parameters, given in Table I in the Appendix, are used except that the proportional gain of the power controller for DG$_2$ (k_{pp}^2) is set to 2. Sim-
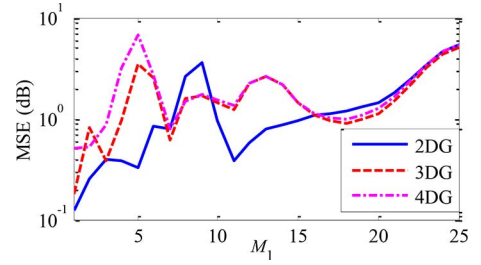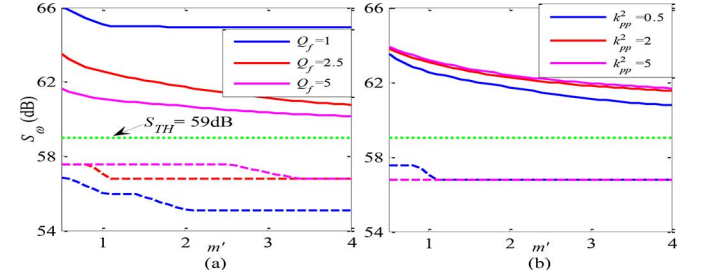
ilar parameters are used for the 3-DG and 4-DG systems with $k_{pp}^3 = 5$ and $k_{pp}^4 = 1$. Also, the load is assumed to be equally shared by all DGs and, hence, P_o^i is set equal to $1/N$ p.u., where N is the number of connected DGs, and i is the DG index. Fig. 7 shows the effect of different M_1 values on MSEs for different numbers of connected DGs. It can be seen from Fig. 7 that a minimum MSE is obtained for all simulated cases at $M_1 = 1$ and, hence, M_1 is set to 1 for the remaining simulations.

For the two-DG system, let us define the load share ratio as $m' = P_o^2/P_o^1$ where $P_o^1 + P_o^2 = 1$ p.u. The droop slopes for the two-DG system are set as follows: $K_\omega^1 = -0.1167$, $K_\omega^2 = -0.0583$, $K_v^1 = -2.2$ and $K_v^2 = -1.1$. The rest of the parameters are similar to Table I, where k_{pp}^1 and k_{pp}^2 are initially set to 0.5. The PMS, described in the Appendix, is implemented for DG$_1$ only while DG$_2$ employs a constant power controller. Fig. 8 shows the effect of m' on $\hat{S}_\omega$ for a two-DG system where $\hat{S}_\omega^1 = \hat{S}_\omega^2 = \hat{S}_\omega$. Fig. 8(a) shows that as the value of m' increases, $\hat{S}_\omega$ decreases and a lower/higher value of $\hat{S}_\omega$ is obtained for larger Q_f value before/after an islanding condition. At $m' = 1$, the stiffness gap is 9.07, 5.49, and 3.51 dB for Q_f value 1, 2.5, and 5, respectively, while at $m' = 4$, the gap is 9.86, 3.97, and 3.34 dB for Q_f value 1, 2.5, and 5, respectively. Fig. 8(b) shows that as m' increases, the value of $\hat{S}_\omega$ decreases where a higher $\hat{S}_\omega$ value is obtained for a larger k_{pp}^2 value. Hence, the PMS provides a higher $\hat{S}_\omega$ value and the use of different control schemes can significantly degrade the overall stiffness of the system when DGs with lower stiffness provide higher power ratio. However, the 59 dB threshold maintains robust islanding detection performance for all simulated cases.

C. Robustness Against Other Power System Disturbances

In this subsection, the performance of the proposed IDM is verified for different types of power system disturbances occurring at different locations across the distribution feeder. In
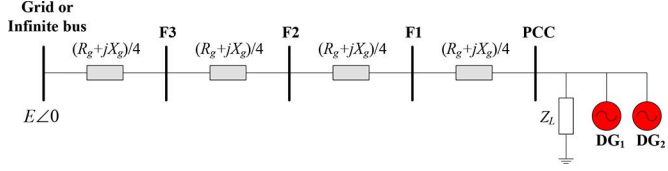
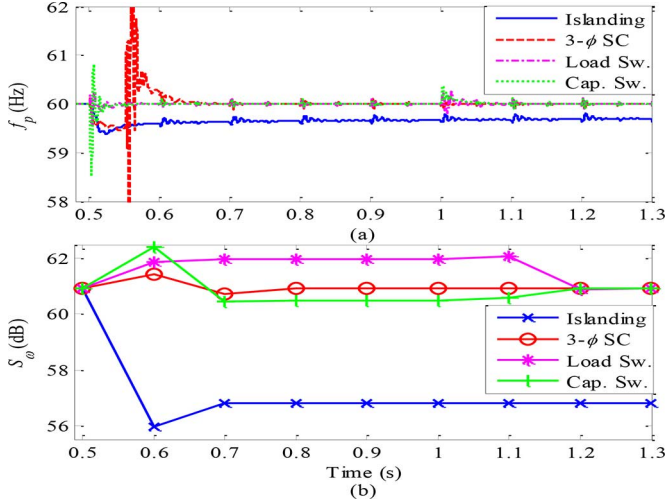Fig. 9. Single-line diagram for studying disturbances at different locations across the distribution feeder.

Fig. 10. (a) PLL frequency response and (b) $\hat{S}_\omega$ during different disturbances at the PCC.
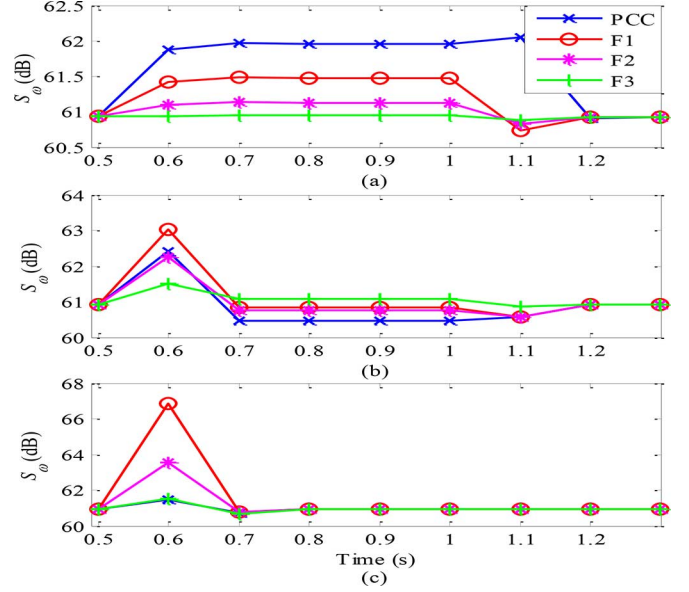

Fig. 11. $\hat{S}_\omega$ for different disturbances at different locations across the distribution feeder. (a) Load switching. (b) Capacitance switching. (c) Three-phase fault.

addition to the islanding condition, the proposed IDM is validated during load variation, capacitance switching, and three-phase-to-ground fault. An average Simulink model of a two-DG system, shown in Fig. 9, is used in simulation. Three different types of disturbances at various locations across the distribution feeder are studied for their effects. The parameters used for the two-DG model are given in Table I except that k_{pp}^2 is set to 2. Also, the droop slopes are set as follows: $K_\omega^1 = -0.1167, K_\omega^2 = -0.0583, K_v^1 = -2.2$ and $K_v^2 = -1.1$. The load power is assumed to be equally shared by both DGs (i.e., $P_o^1 = P_o^2 = 0.5$ p.u.). The following types of disturbances are investigated: 1) an islanding condition is simulated by disconnecting the circuit breaker (CB) at $t = 0.5$ s; 2) a three-phase-to-ground fault at $t = 0.5$ s and clears out within 0.05 s; 3) an additional load, with apparent power equal to $1 + j1$ p.u., is switched on at $t = 0.5$ s and off at $t = 1$ s; and 4) a capacitance, with reactive power equal to 1 p.u., is switched on at $t = 0.5$ s and off at $t = 1$ s. Cases 2)–4) are carried out at various locations across the distribution feeder.

The overall stiffness of the two-DG system is estimated every 0.1 s. Fig. 10 shows the frequency response and $\hat{S}_\omega$ during different types of power system disturbances taking place at PCC. Results from Fig. 10(b) show that $\hat{S}_\omega$ changes from 60.93 to 56.79 dB with an overshoot of -0.83 dB during the islanding condition. For the three-phase short circuit fault, $\hat{S}_\omega$ slightly changes to 61.44 dB and then oscillates until it settles back to 60.93 dB at $t = 0.8$ s. For the load and capacitance switching cases, the stiffness measure increases/decreases when additional load/capacitance is switched on, respectively. The value of $\hat{S}_\omega$ is increased to 61.96 dB when the additional load is switched on,

while the $\hat{S}_\omega$ value decreases to 60.47 dB with a large overshoot of 1.94 dB when the capacitance is switched on. The initial value of $\hat{S}_\omega$ is recovered within 0.2 s after the additional load/capacitance is switched off. Fig. 11 shows the values of $\hat{S}_\omega$ in the presence of power system disturbances at various locations across the distribution feeder. It can be seen from Fig. 11 that the stiffness value experiences a larger change when the load switching takes place at locations closer to PCC. Also, similar observations can be made for capacitance switching and three-phase fault, that is, disturbances further away from the PCC result in a smaller change in the stiffness value. Despite the differences, the threshold of 59 dB can successfully and consistently distinguish an islanding condition under different types of disturbances occurring at various locations across the distribution feeder. In other words, the proposed technique has robust performance against all possible disturbances illustrated in Fig. 9.

D. Applicability to Multi-Microgrid Structures

In this subsection, the performance of the proposed IDM is studied for cases that DGs form evolving microgrids and some of the microgrids get disconnected from the grid while the rest remain connected. Such a multi-microgrid structure is shown in Fig. 12, and it consists of two microgrids (MG_1 and MG_2), each of the microgrids consists of two DGs and a local load. A circuit breaker (CB_{12}) is used to simulate an islanding condition for MG_2 only. Z_{line}^{12} is the impedance of the line that connects MG_1 to MG_2, and the bus voltages across MG_1 and MG_2 are denoted by v_1 and v_2, respectively. The parameters used in Fig. 12 are as follows: $Z_{\text{line}}^{12} = 0.01 + j0.01\Omega$ and $Z_L^1 = Z_L^2 = 2Z_L$, where Z_L is the RLC load impedance given in Table I. The rest of parameters are also provided by Table I except that $N = 4, k_{\text{pp}}^2 = k_{\text{pp}}^4 = 2, K_\omega^2 = K_\omega^4 = -0.1167, K_v^2 = K_v^4 = -2.2$, and $P_o^i = 0.25$ p.u., where $i = 1, 2, 3, 4$. Two cases are simulated. In the first case, the main circuit breaker CB is disconnected at $t = 0.5$ s to simulate an islanding condition for all
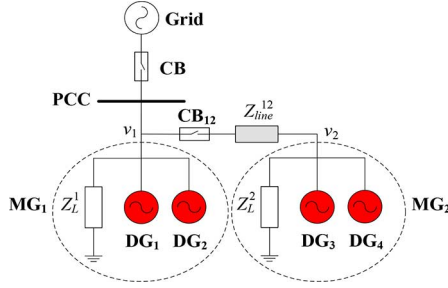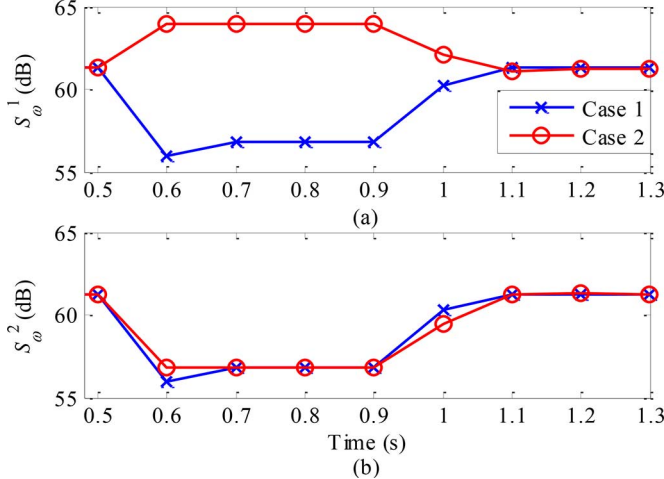
Fig. 12.　Schematic diagram for the two-microgrid structure under study.

Fig. 13.　$\hat{S}_\omega$ under different microgrid formation for (a) MG_1 and (b) MG_2.

DGs, and then CB is closed at $t = 0.9$ s. As for the second case, only CB_{12} is disconnected at $t = 0.5$ s to simulate an islanding condition for MG_2, and then CB_{12} is reconnected to the grid at $t = 0.9$ s. Fig. 13 shows the stiffness values of both microgrid buses for both cases. $\hat{S}_\omega^1$ and $\hat{S}_\omega^2$ are the estimated stiffness measures at MG_1 and MG_2, respectively. The results in Fig. 13 illustrate that both DGs within disconnected microgrid(s) detect the islanding condition. In case 1, where CB is disconnected, $\hat{S}_\omega^1$ changes from 61.28 dB to 56.79 dB and $\hat{S}_\omega^2$ changes from 61.21 dB to 56.79 dB. The initial values of $\hat{S}_\omega$ are recovered within 0.2 s after CB is reconnected to the grid. On the other hand, an islanding condition is detected for case 2 by the two DGs within MG_2 only (DG_3 and DG_4) since $\hat{S}_\omega^2$ changes from 61.21 dB to 56.79 dB while $\hat{S}_\omega^1$ increases to 63.92 dB upon CB_{12} being disconnected. The initial $\hat{S}_\omega$ values are recovered within 0.2 s when MG_2 is reconnected to grid. Again, the threshold of 59 dB can successfully distinguish these islanding conditions within the multi-microgrid structure, and the proposed technique is robust in islanding detection when some of the DGs are disconnected while others remain connected to the grid.

Finally, it is important to highlight several very important differences between the proposed technique in this paper versus previously proposed islanding detection techniques in the literature. First, the vast majority (if not all) of active IDMs (for example, [5] to [15]) are for DGs equipped with a constant current or constant power DG interface. On the contrary, this work attempts to address a much more challenging problem of detecting islanding for DGs with droop control. Typically, active IDMs try
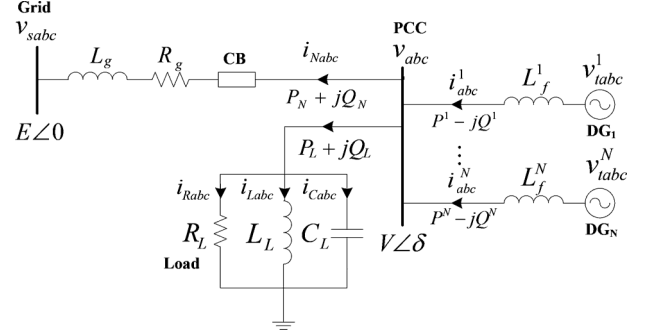

Fig. 14.　Single-line schematic diagram of a multi-DG system.

to de-stabilize the system while on the contrary droop control would try to stabilize. Their conflicting objectives would have an adverse effect on islanding detection. In comparison with all other IDMs, the main advantages of the proposed approach are:
1)　Detecting islanding for microgrids with droop control.
2)　The perturbations injected by the proposed method have no effect on the stability of the microgrid equipped with droop control.
3)　This is coupled with the advantage of having negligible NDZ.

V. CONCLUSION

In this paper, a new active IDM is proposed for multi-DG systems. The proposed technique depends on estimating an overall transient stiffness measure, which is defined in terms of the transfer function infinity-norm for such DG system. Each DG is required to perturb at distinct frequencies from other DGs to avoid spectrum overlapping and, hence, no communications are required among the DGs. The estimated stiffness value is then used to determine the status of the grid where a clear separation between prior- and post-islanding stiffness is obtained. Results show that the proposed technique is scalable and robust against different loading conditions, variations in grid stiffness level, number of connected DGs, and different types of DG controllers. Furthermore, the proposed technique can distinguish islanding condition from other types of power system disturbances such as three-phase-to-ground fault, capacitance switching, and load variations.

APPENDIX A
DERIVATION OF MULTI-DG SMALL-SIGNAL MODEL

For simulation purposes, the general N-DG system shown in Fig. 14 is considered where N is the number of connected DGs. In Fig. 14, all DGs are directly connected to the PCC and, hence, the DG's bus voltage is the PCC voltage. L_g and R_g correspond to the inductance and resistance of the utility line, respectively. The grid voltage is v_{sabc} or $E \angle 0$ and the PCC voltage is v_{abc} or $V \angle \delta$. The inductance of the ith inverter filter is represented by L_f^i. $(P_N + jQ_N)$ is the power imbalance between the parallel RLC load $(P_L + jQ_L)$ and the total power output supplied by all DGs. The current absorbed by the grid is i_{Nabc}. For the parallel RLC load, i_{Rabc}, i_{Labc}, and i_{Cabc} are the resistance, inductance, and capacitance currents, respectively. In this model, an average model for the three-phase voltage-source inverter (VSI)
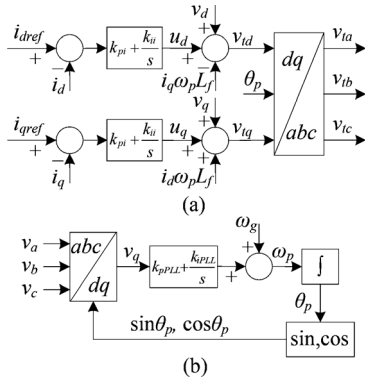
Fig. 15. Block diagrams of controller of a single DG system. (a) Constant current controller. (b) Three-phase PLL.
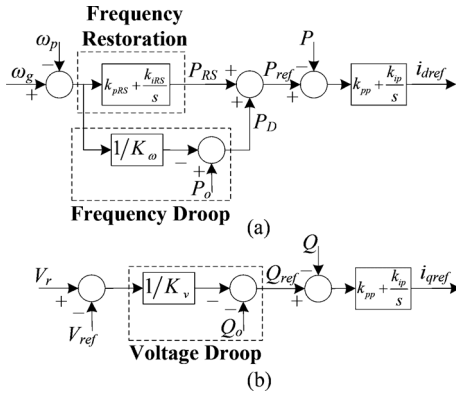

Fig. 16. Block diagrams of the microgrid power-management controller. (a) Active power controller. (b) Reactive power controller.

is employed where the pulsewidth-modulated (PWM) signal generator, the dc source, and the switching power electronics devices are replaced by a three-phase controlled voltage source [8], [14]. A PLL is used to measure the frequency of the PCC voltage.

A. Typical Controller for Single DG System

Fig. 15 shows the details of the typical current controller and the PLL blocks used in each DG's control scheme. The current controller is shown in Fig. 15(a). i_{dref} and i_{qref} are the d- and q-axis current references, respectively. The angle used in the dq transformation (θ_p) is measured by a PLL, with proportional-integral (PI) controller gains k_{pPLL} and k_{iPLL}, as shown in Fig. 15(b). Then, the current references are subtracted from measured output currents (i_d and i_q) and applied to PI controllers with gains k_{pi} and k_{ii}, respectively. The d- and q-axis outputs of the current controller are u_d and u_q, respectively. Adding $v_d - i_q\omega_p L_f$ to u_d and $v_q + i_d\omega_p L_f$ term to u_q is known as cross-coupling which is used to decouple control equations. Finally, a dq-abc transformation is applied to construct three-phase voltage signal (v_{tabc}) which is used to drive the controlled voltage sources shown in Fig. 14.

B. Microgrid Power-Management Strategy (PMS)

The active/reactive PMS proposed in [16] is used to support the frequency and voltage of the microgrid. The proposed strategy includes a frequency-restoration term, and frequency/

TABLE I
MULTI-DG SMALL-SIGNAL MODEL PARAMETERS

Parameters	Value	Parameters	Value
S_B, I_B	10 kVA, 39.3 A	$k_{pPLL}{}^i, k_{iPLL}{}^i$	50, 500
E, V_B	169.7 V	$k_{pi}{}^i, k_{ii}{}^i$	0.5, 50
$f_g, f_{min}{}^i$	60, 59.3 Hz	$k_{pp}{}^i, k_{ip}{}^i$	0.5, 50
R_g, L_g	0.11 Ω, 0.44 mH	$k_{pRS}{}^i, k_{iRS}{}^i$	0.5, 5
R_L, C_L	4.32 Ω,1.54 mF	$V_{min}{}^i, V_{max}{}^i$	0.88, 1.1 p.u.
$L_L, L_f{}^i$	4.58 mH, 1 mH	$P_{max}{}^i, Q_{max}{}^i$	1.2/N, 0.2/N p.u.
$V_{ref}{}^i$	1 p.u.	$K_\omega{}^i, K_v{}^i$	−0.058N, −1.1N

voltage droop blocks in addition to the typical power regulator as shown in Fig. 16. In Fig. 16, the frequency error is applied to a PI controller, with gains k_{pRS} and k_{iRS}, to obtain P_{RS}. P_{RS} is added to P_D to obtain the real power reference of the power regulator block (P_{ref}) where P_D is generated by the frequency droop control. On the other hand, Q_{ref} is generated by the voltage droop control as shown in Fig. 16(b) where V_r is the measured rms voltage. Then, the generated power references (P_{ref} and Q_{ref}) are subtracted from the measured power (P and Q) and fed into a PI controller (with gains k_{pp} and k_{ip}) to generate i_{dref} and i_{qref}, respectively, which are used as inputs to the current controller shown in Fig. 15(a). The frequency and voltage droop slopes can be calculated as follows:

$$K_\omega = \frac{1 - \omega'_{min}}{P_o - P_{max}}, \quad K_v = \frac{V_{max} - V_{min}}{-Q_{max}}, \quad (12)$$

where V_{max} and V_{min} are the per-unit maximum and minimum permissible voltage, respectively; $\omega'_{min} = 2\pi f_{min}/\omega_g$; and P_o is the initial active power assigned to the DG. P_{max} and Q_{max} are the per-unit maximum active and reactive power of the DG, respectively. Utilizing PMSs interfere with active IDMs, and the islanding condition will become more difficult to detect.

C. Small-Signal Model of the Multi-DG System

To simplify the multi-DG model, the PLL controller gains, used at each DG, are assumed to be the same. Hence, the total number of state variables in the overall system is reduced from $14N$ to $6N + 8$. Accordingly, the small-signal model of the multi-DG system is described by (13), shown at the top of the next page, where $a_{1,1} = R_L^{-1}C_L^{-1}, a_{1,3} = Z_B^{-1}C_L^{-1}, \mathbf{c}_1 = Z_B\mathbf{L}_f^{-1}\mathbf{k}_{pi}, \mathbf{a}_{3,1} = \mathbf{c}_1\mathbf{k}_{pp}\mathbf{i}_{d0}\mathbf{1}, \mathbf{a}_{3,2} = -\mathbf{c}_1\mathbf{k}_{pp}\mathbf{i}_{q0}\mathbf{1}, \mathbf{a}_{3,3} = \mathbf{c}_1(\mathbf{k}_{pp}v_{d0} + \mathbf{I}), \mathbf{a}_{3,4} = -\mathbf{c}_1\mathbf{k}_{pp}v_{q0}, \mathbf{a}_{3,9} = Z_B\mathbf{L}_f^{-1}\mathbf{k}_{ii}, \mathbf{a}_{3,11} = \mathbf{c}_1\mathbf{k}_{ip}, \mathbf{a}_{3,13} = \mathbf{c}_1\mathbf{k}_{pp}k_{iRS}\mathbf{1}\omega_g^{-1}, \mathbf{a}_{3,14} = \mathbf{c}_1\mathbf{k}_{pp}(k_{pRS} + \mathbf{K}_\omega^{-1})\mathbf{1}\omega_g^{-1}, \mathbf{a}_{4,1} = -\mathbf{c}_1\mathbf{k}_{pp}(\mathbf{i}_{q0} + \mathbf{K}_v^{-1}V_{r0}^{-1}v_{d0})\mathbf{1}, \mathbf{a}_{4,2} = \mathbf{c}_1\mathbf{k}_{pp}(\mathbf{i}_{d0} - \mathbf{K}_v^{-1}V_{r0}^{-1}v_{q0})\mathbf{1}, a_{5,1} = Z_BL_g^{-1}, a_{5,5} = R_gL_g^{-1}, a_{5,13} = Z_BL_g^{-1}E\sin\delta_0, a_{6,13} = Z_BL_g^{-1}E\cos\delta_0, a_{7,1} = Z_BL_L^{-1}, \mathbf{a}_{9,l} = \mathbf{c}_1^{-1}\mathbf{a}_{3,l}, \mathbf{a}_{10,m} = \mathbf{c}_1^{-1}\mathbf{a}_{4,m}, l = 1, 2, 3, 4, 11, 13, 14, m = 1, 2, \mathbf{a}_{11,13} = \mathbf{k}_{iRS}\mathbf{1}\omega_g^{-1}, \mathbf{a}_{11,14} = (\mathbf{k}_{pRS} - \mathbf{K}_\omega^{-1})\mathbf{1}\omega_g^{-1}, \mathbf{a}_{12,1} = -(\mathbf{i}_{q0} + \mathbf{K}_v^{-1}V_{r0}^{-1}v_{d0})\mathbf{1}, \mathbf{a}_{12,2} = (\mathbf{i}_{d0} - \mathbf{K}_v^{-1}V_{r0}^{-1}v_{q0})\mathbf{1}, a_{14,1} = k_{pPLL}\omega_{p0}, a_{14,2} = k_{pPLL}R_L^{-1}C_L^{-1} - k_{iPLL}, a_{14,4} = k_{pPLL}Z_B^{-1}C_L^{-1}, a_{14,14} = k_{pPLL}v_{d0}, \mathbf{b}_{3,1} = \mathbf{c}_1\mathbf{k}_{pp}, Z_B = V_B/I_B$ is the base impedance, $\mathbf{1} = [1\ldots1]^T \in \Re^{N\times1}, \mathbf{I}$ is the $N \times N$ identity matrix, p is the derivative operator, Δ is the small-signal variable, and variables with subscript 0 are the steady-state values. Also, the small-signal variables highlighted in bold are vectors with N

$$
\begin{cases}
p\Delta v_d = -a_{1,1}\Delta v_d + \omega_{p0}\Delta v_q + a_{1,3}\mathbf{1}^T\Delta i_d - a_{1,3}\Delta i_{Nd} - a_{1,3}\Delta i_{Ld} + v_{q0}\Delta\omega_p \\
p\Delta v_q = -\omega_{p0}\Delta v_d - a_{1,1}\Delta v_q + a_{1,3}\mathbf{1}^T\Delta i_q - a_{1,3}\Delta i_{Nq} - a_{1,3}\Delta i_{Lq} - v_{d0}\Delta\omega_p
\end{cases}
$$

$$
\begin{cases}
p\Delta\mathbf{i}_d = -\mathbf{a}_{3,1}\Delta v_d + \mathbf{a}_{3,2}\Delta v_q - \mathbf{a}_{3,3}\Delta\mathbf{i}_d + \mathbf{a}_{3,4}\Delta\mathbf{i}_q + \mathbf{a}_{3,9}\Delta\mathbf{i}_{ud} + \mathbf{a}_{3,11}\Delta\mathbf{p}_d - \mathbf{a}_{3,13}\Delta\delta_p - \mathbf{a}_{3,14}\Delta\omega_p + \mathbf{b}_{3,1}\Delta\mathbf{P}_o
\end{cases}
$$

$$
\begin{cases}
p\Delta\mathbf{i}_q = \mathbf{a}_{4,1}\Delta v_d + \mathbf{a}_{4,2}\Delta v_q - \mathbf{a}_{3,4}\Delta\mathbf{i}_d - \mathbf{a}_{3,3}\Delta\mathbf{i}_q + \mathbf{a}_{3,9}\Delta\mathbf{i}_{uq} + \mathbf{a}_{3,11}\Delta\mathbf{q}_q - \mathbf{b}_{3,1}\Delta\mathbf{Q}_o
\end{cases}
$$

$$
\begin{cases}
p\Delta i_{Nd} = a_{5,1}\Delta v_d - a_{5,5}\Delta i_{Nd} + \omega_{p0}\Delta i_{Nq} + a_{5,13}\Delta\delta_p + i_{Nq0}\Delta\omega_p \\
p\Delta i_{Nq} = a_{5,1}\Delta v_q - \omega_{p0}\Delta i_{Nd} - a_{5,5}\Delta i_{Nq} + a_{6,13}\Delta\delta_p - i_{Nd0}\Delta\omega_p
\end{cases}
$$

$$
\begin{cases}
p\Delta i_{Ld} = a_{7,1}\Delta v_d + \omega_{p0}\Delta i_{Lq} + i_{Lq0}\Delta\omega_p \\
p\Delta i_{Lq} = a_{7,1}\Delta v_q - \omega_{p0}\Delta i_{Ld} - i_{Ld0}\Delta\omega_p
\end{cases}
$$

$$
\begin{cases}
p\Delta\mathbf{i}_{ud} = -\mathbf{a}_{9,1}\Delta v_d + \mathbf{a}_{9,2}\Delta v_q - \mathbf{a}_{9,3}\Delta\mathbf{i}_d + \mathbf{a}_{9,4}\Delta\mathbf{i}_q + \mathbf{a}_{9,11}\Delta\mathbf{p}_d - \mathbf{a}_{9,13}\Delta\delta_p - \mathbf{a}_{9,14}\Delta\omega_p + \mathbf{k}_{\mathrm{pp}}\Delta\mathbf{P}_o
\end{cases}
$$

$$
\begin{cases}
p\Delta\mathbf{i}_{uq} = \mathbf{a}_{10,1}\Delta v_d + \mathbf{a}_{10,2}\Delta v_q - \mathbf{a}_{9,4}\Delta\mathbf{i}_d - \mathbf{a}_{9,3}\Delta\mathbf{i}_q + \mathbf{a}_{9,11}\Delta\mathbf{q}_q - \mathbf{k}_{\mathrm{pp}}\Delta\mathbf{Q}_o
\end{cases}
$$

$$
\begin{cases}
p\Delta\mathbf{p}_d = -\mathbf{i}_{d0}\mathbf{1}\Delta v_d - \mathbf{i}_{q0}\mathbf{1}\Delta v_q - v_{d0}\mathbf{I}\Delta\mathbf{i}_d - v_{q0}\mathbf{I}\Delta\mathbf{i}_q - \mathbf{a}_{11,13}\Delta\delta_p - \mathbf{a}_{11,14}\Delta\omega_p + \Delta\mathbf{P}_o
\end{cases}
$$

$$
\begin{cases}
p\Delta\mathbf{q}_q = \mathbf{a}_{12,1}\Delta v_d + \mathbf{a}_{12,2}\Delta v_q + v_{q0}\mathbf{I}\Delta\mathbf{i}_d - v_{d0}\mathbf{I}\Delta\mathbf{i}_q - \Delta\mathbf{Q}_o
\end{cases}
$$

$$
\begin{cases}
p\Delta\delta_p = \Delta\omega_p \\
p\Delta\omega_p = -a_{14,1}\Delta v_d - a_{14,2}\Delta v_q + a_{14,4}\mathbf{1}^T\Delta\mathbf{i}_q - a_{14,4}\Delta i_{Nq} - a_{14,4}\Delta i_{Lq} - a_{14,14}\Delta\omega_p
\end{cases} \tag{13}
$$

elements. For example, the d-axis measured current has the following definition:

$$
\Delta\mathbf{i}_d = [\Delta i_d^1 \quad \Delta i_d^2 \ldots \Delta i_d^N]^T.
$$

In addition, $\mathbf{i}_{d0}, \mathbf{i}_{q0}, \mathbf{k}_{pi}, \mathbf{k}_{ii}, \mathbf{k}_{pp}, \mathbf{k}_{ip}, \mathbf{k}_{pRS}, \mathbf{k}_{iRS}, \mathbf{K}_\omega, \mathbf{K}_v,$ and $\mathbf{L}_f$ are diagonal matrices. For illustration, $\mathbf{K}_\omega$ is defined as $\mathrm{diag}\{K_\omega^i\}$ with $i = 1, 2, \ldots, N$. All currents, voltages, and powers in (14) are transformed to per unit [25]. Then, the overall system can be written as follows:

$$
p\Delta\mathbf{x} = \mathbf{A}\Delta\mathbf{x} + \mathbf{B}\Delta\mathbf{u} \tag{14}
$$

where $\Delta\mathbf{x} = [\Delta v_d \Delta v_q \Delta\mathbf{i}_d^T \ \Delta\mathbf{i}_q^T \Delta i_{Nd}\Delta i_{Nq}\Delta i_{Ld}\Delta i_{Lq} \ \Delta\mathbf{i}_{ud}^T \ \Delta\mathbf{i}_{uq}^T \ \Delta\mathbf{p}_d^T \ \Delta\mathbf{q}_q^T \ \Delta\delta_p \ \Delta\omega_p]^T$, $\Delta\mathbf{u} = [\Delta\mathbf{P}_o^T \Delta\mathbf{Q}_o^T]^T$, and $\mathbf{A}$ and $\mathbf{B}$ are constructed from (14). Further details on the derivation of this model can be found in [18] and [26]. Table I shows the parameters used for the multi-DG model.

REFERENCES

[1] *IEEE Recommended Practice for Utility Interface of Photovoltaic (PV) Systems*, IEEE Standard 929–2000, Apr. 2000.

[2] *IEEE Standard for Interconnecting Distributed Resources With Electric Power Systems*, IEEE Standard 1547-2003, Jul. 2003.

[3] W. Bower and M. Ropp, Evaluation of islanding detection methods for photovoltaic utility-interactive power systems Rep. IEA-PVPS T5-09:2002, Mar. 2002.

[4] B. Yu, M. Matsui, and G. Yu, "A review of current anti-islanding methods for photovoltaic power system," *Solar Energy*, vol. 84, no. 5, pp. 745–754, May 2010.

[5] L. Lopes and H. Sun, "Performance assessment of active frequency drifting islanding detection methods," *IEEE Trans. Energy. Convers.*, vol. 21, no. 1, pp. 171–180, Mar. 2006.

[6] B. Bahrani, H. Karimi, and R. Iravani, "Nondetection zone assessment of an active islanding detection method and its experimental evaluation," *IEEE Trans. Power Del.*, vol. 26, no. 2, pp. 517–525, Apr. 2011.

[7] G. Gonzalez and R. Iravani, "Current injection for active islanding detection of electronically-interfaced distributed resources," *IEEE Trans. Power Del.*, vol. 21, no. 3, pp. 1698–1705, Jul. 2006.

[8] X. Wang and W. Freitas, "Impact of positive-feedback anti-islanding methods on small-signal stability of inverter-based distributed generation," *IEEE Trans. Energy Convers.*, vol. 23, no. 3, pp. 923–931, Sep. 2008.

[9] X. Wang, W. Freitas, V. Dinavahi, and W. Xu, "Investigation of positive feedback anti-islanding control for multiple inverter-based distributed generators," *IEEE Trans. Power Syst.*, vol. 24, no. 2, pp. 785–795, May 2009.

[10] L. Lopes and Y. Zhang, "Islanding detection assessment of multi-inverter systems with active frequency drifting methods," *IEEE Trans. Power Del.*, vol. 23, no. 1, pp. 480–486, Jan. 2008.

[11] H. Zeineldin and S. Conti, "Sandia frequency shift parameter selection for multi-inverter systems to eliminate non-detection zone," *IET Renew. Power Gen.*, vol. 5, no. 2, pp. 175–183, Mar. 2011.

[12] E. Estebanez *et al.*, "Performance evaluation of active islanding detection algorithms in distributed-generation photovoltaic systems: two inverters case," *IEEE Trans. Ind. Electron.*, vol. 58, no. 4, pp. 1185–1193, Apr. 2011.

[13] H. Zeineldin, E. El-Saadany, and M. Salama, "Impact of DG interface control on islanding detection and nondetection zones," *IEEE Trans. Power Del.*, vol. 21, no. 3, pp. 1515–1523, Jul. 2006.

[14] X. Wang, W. Freitas, and W. Xu, "Dynamic non-detection zones of positive feedback anti-islanding methods for inverter-based distributed generators," *IEEE Trans. Power Del.*, vol. 26, no. 2, pp. 1145–1155, Apr. 2011.

[15] X. Wang, W. Freitas, W. Xu, and V. Dinavahi, "Impact of DG interface controls on the sandia frequency shift anti-islanding method," *IEEE Trans. Energy Convers.*, vol. 22, no. 3, pp. 792–794, Sep. 2007.

[16] F. Katiraei and M. Iravani, "Power management strategies for a microgrid with multiple distributed generation units," *IEEE Trans. Power Syst.*, vol. 21, no. 4, pp. 1821–1831, Nov. 2006.

[17] F. Gao and M. Iravani, "A control strategy for a distributed generation unit in grid-connected and autonomous modes of operation," *IEEE Trans. Power Del.*, vol. 23, no. 2, pp. 850–859, Apr. 2008.

[18] X. Wang, "Investigation of positive feedback anti-islanding scheme for inverter-based distributed generation," Ph.D. dissertation, Dept. Elect. Comput. Eng., Univ. Alberta, Edmonton, AB, Canada, 2008.

[19] H. Zeineldin, E. El-Saadany, and M. Salama, "Intentional islanding of distributed generation," in *Proc. IEEE Power Energy Soc. Gen. Meeting*, Jun. 12–16, 2005, vol. 2, pp. 1496–1502.

[20] I. Balaguer, Q. Lei, S. Yang, U. Supatti, and F. Peng, "Control for grid-connected and intentional islanding operations of distributed power generation," *IEEE Trans. Ind. Electron.*, vol. 58, no. 1, pp. 147–157, Jan. 2011.

[21] Y. Mohamed and E. El-Saadany, "Adaptive decentralized droop controller to preserve power sharing stability of paralleled inverters in distributed generation microgrids," *IEEE Trans. Power Electron.*, vol. 23, no. 6, pp. 2806–2816, Nov. 2008.

[22] J. Guerrero, J. Matas, L. Vicuna, M. Castilla, and J. Miret, "Decentralized control for parallel operation of distributed generation inverters using resistive output impedance," *IEEE Trans. Ind. Electron*, vol. 54, no. 2, pp. 994–1004, Apr. 2007.

[23] J. Bloemink and M. Iravani, "Control of a multiple source microgrid with built-in islanding detection and current limiting," *IEEE Trans. Power Del.*, vol. 27, no. 4, pp. 2122–2132, Oct. 2012.

[24] R. Qi, F. Coakley, and B. Evans, "Practical consideration for bandpass sampling," *Electron. Lett.*, vol. 32, no. 20, pp. 1861–1862, Sep. 1996.

[25] C. Schauder and H. Mehta, "Vector analysis and control of advanced static VAR compensators," *Proc. Inst. Elect. Eng., Gen., Transm. Distrib.*, vol. 140, no. 4, pp. 299–306, Jul. 1993.

[26] M. Al Hosani, "Transient and distributed algorithms to improve islanding detection capability of inverter based distributed generation," Ph.D. dissertation, Dept. Elect. Eng. Comput. Sci., Univ. Central Florida, Orlando, FL, USA, 2013.

Zhihua Qu (M'90–SM'93–F'09) received the Ph.D. degree in electrical engineering from the Georgia Institute of Technology, Atlanta, GA, USA, in 1990.

Since then, he has been with the University of Central Florida, Orlando, FL, USA. Currently, he is the SAIC Endowed Professor with the College of Engineering and Computer Science, a Professor and the Chair of Electrical and Computer Engineering, and the Director of FEEDER Center (one of DoE-funded national centers on distributed technologies and smart grid). His areas of expertise are nonlinear systems and control, with applications to energy and power systems. In energy systems, his research covers such subjects as low-speed power generation, dynamic stability of distributed power systems, anti-islanding control and protection, distributed generation and load sharing control, distributed VAR compensation, distributed optimization, and cooperative control.

Mohamed Al Hosani (S'10–M'13) received the B.Sc. degree in electrical engineering from the American University of Sharjah, United Arab Emirates, in 2008 and the M.Sc. and the Ph.D. degrees in electrical engineering from the University of Central Florida, Orlando, FL, USA, in 2010 and 2013, respectively.

Currently, he is an Assistant Professor with the Masdar Institute, United Arab Emirates. His current interests include the anti-islanding algorithm and microgrid stability analysis.

H. H. Zeineldin (M'08–SM'13) received the B.Sc. and M.Sc. degrees in electrical engineering from Cairo University, Cairo, Egypt, in 1999 and 2002, respectively, and the Ph.D. degree in electrical and computer engineering from the University of Waterloo, Waterloo, ON, Canada, in 2006.

He is an Associate Professor with the Masdar Institute, United Arab Emirates. He is currently an Editor of the IEEE TRANSACTIONS ON ENERGY CONVERSION and of the IEEE TRANSACTIONS ON SMART GRIDS. His current interests include power system protection, microgrids, and distributed generation.